IEEE Access
Multidisciplinary | Rapid Review | Open Access Journal

Received October 5, 2020, accepted November 1, 2020, date of publication November 9, 2020, date of current version November 19, 2020.

Digital Object Identifier 10.1109/ACCESS.2020.3036884

A Compact High-Resolution Resonance-Based Capacitive Sensor for Defects Detection on PCBAs

TIE QIU[1,2], (Member, IEEE), CHOON KAIT ANDREW TEK[2], AND SHAO YING HUANG[1], (Member, IEEE)

[1]Engineering Product Development Pillar, Singapore University of Technology and Design, Singapore 487372
[2]Electronic Industrial Solutions Group-Centers of Excellence, Keysight Technologies, Singapore 768923

Corresponding author: Shao Ying Huang (huangshaoying@sutd.edu.sg)

This work was supported by the Keysight Technologies - SUTD collaboration.

ABSTRACT Increased density of printed circuit board assembles (PCBAs) is diminishing physical contact test access of the in-circuit testing (ICT) solutions for defects detection. As a result, it is necessary to design contactless test solutions with high spatial resolution to overcome the current test limitations. In this paper, a compact contactless sensor is presented for monitoring the fabrication quality of PCBAs. The sensor consists of an inductor-capacitor-(LC)-based resonant circuit and it can detect defects on metallic traces of PCBAs in close proximity without a contact. The sensor is designed such that, strong electric field is confined around the sensor tip, which creates strong capacitive coupling between the sensor tip and devices under test (DUTs) within a small region for sensing, i.e. high resolution sensing. The sensitivity of the proposed sensor is verified by the simulated and experimental 2D surface mapping results with sample DUTs, and it shows that the sensor can detect the open or short defects with a size as small as 0.15 mm $\times$ 0.2 mm. Circuit models are proposed to predict the sensing behavior and for guiding the design. The proposed sensor shows great potential to be used in the real-time monitoring of defects along the manufacturing supply chain.

INDEX TERMS In-circuit testing (ICT), printed circuit board (PCB), printed circuit board assembly (PCBA), sensing, near-field sensing, non-destructive evaluation (NDE), capacitive sensors.

I. INTRODUCTION

Electronics manufacturers are continually challenged to ensure sufficient test coverage for their electronic products. In-circuit testing (ICT) [1], [2] has been a gold standard for around 40 years where defects, e.g. open and short of joints, can be detected and fixed in time. Physical contacts to the soldering points are necessary to facilitate a test. However, increasing density of the printed circuit board assembles (PCBAs) is diminishing these physical contacts [3], and ICT becomes less and less feasible and functional testing is heavily relied on. Functional testing [4] is an essential buy-off of any products and only allows an overall/global fault detection, leaving behind the information on which components on the products cause the failure. As a result, a failed PCBA is discarded rather than having the failed components fixed, which causes a large amount of electronic wastage and is environmentally unsound. To obtain a detailed and localized evaluation of a PCBA so that defects can be fixed, non-contact and non-destructive sensing without powering up the PCBAs become critical. Besides, for such an evaluation on PCBAs, a 1D spatial resolution of around 0.15 mm is needed to distinguish different pins of a package for example [5]. In recent years, different potential sensing technologies have been advanced with the development of different probing techniques [6]–[13] to evaluate the fabrication quality of a PCBA, i.e. the device under test (DUT). For example, the X-ray methods have long penetration depth and high spatial resolution, but it needs high cost and possibly result with the radiation hazards [6], [7]. An alternative inspection technique for high density PCBAs is the thermography methods [8], [9]. It has the advantages such as easy operation and simple testing reconfiguration. But the DUT has to be powered up, and this method is susceptible to both non uniform heating and temporal temperature variations, which leads to unreliable sensitivity. Moreover, the acoustic method [10], [11] has excellent long-range diagnostic capability and it is suitable to detect defects on large structures such as pipelines, marine,

The associate editor coordinating the review of this manuscript and approving it for publication was Francesco Tedesco.

ships, and aerospace, but for small and complex DUTs like PCBAs, it faces the challenge from heavy data processing and a large number of sensors could be needed. Among these techniques, near-field radio frequency (RF) non-destructive evaluation (NDE) offers advantages of single-side access, contactless, low cost, and high measurement speed [12], [13].

The near-field RF NDE testing methods can be categorized based on the type of fields used for sensing, the electric-field (E-field) sensing [12]–[23], and magnetic-field (H-field) sensing [24]–[29]. For E-field sensing, a popular method is open-ended coaxial probing [14]–[17]. It is widely used for in vivo measurements of permittivity of biological tissues for medical imaging and diagnostics. The permittivity of the material can be extracted from the measured reflection coefficients (S_{11}) when an open-ended coaxial transmission line is in contact with the surface of the DUT. The typical spatial resolution of this method depends on the physical size of the opening of the coaxial cables, which lies in the range from a few millimetres to a few centimetres. For a higher spatial resolution, cavity resonance technique was proposed in [18], [19] for measuring surface dielectric properties, typically in the micrometer to sub-micrometer range. For this method, the measurement is based on the perturbation of the resonance of a coaxial cavity through a probe tip mounted to the center conductor of an coaxial cable attached to the aperture in the end wall of the resonator. The probe's metal tip is sharpened to obtain a high spatial resolution. However, the sharpen tip is sensitive to vibration and thus a sophisticated anti-vibration system is needed for the measurement, which dramatically increases both the complexity and the cost of the measurement. Recently, split-ring resonators (SRRs) have been applied for near-field sensing [13], [20], [21]. The sensing is conducted through the strong electrical field at the slit of the ring where the size of the slit decides the spatial resolution of sensing. A DUT placed near the slit changes the resonant frequency due to its electrical properties, thus the electrical properties can be deduced from the measured shifted of resonant frequencies [13], [20], [21]. For a high spatial resolution, the size of the SRR has to be reduced, which increases the resonant frequency and subsequently the cost of the driving circuit. Another existing near-field sensing solution is open-ended waveguide slit based on the shift of resonant frequency [22], [23]. Although the waveguide slit can provide a resolution of better than 0.1 mm, it has to operate at a high frequency for a high resolution, which increases the cost of the testing instrumentation. Sensing using the E-field of a capacitor is another approach where a parallel-plate capacitor is used to form a resonator with a lumped inductor [12]. The spatial resolution of such a sensor is determined by the physical size of the capacitor. For example in [12], the resolution is limited at 3 mm.

For H-field sensing [24]–[29], it mainly relies on the eddy current testing (ECT) method, which has been utilized in NDE for a long time and widely applied to inspect conductive material structure in order to verify their structural integrity. For the principle of the ECT, it can be summarized as follows. The exciting signal produces the principal magnetic flux through the excitation coils. Then the principal magnetic flux induces the eddy current (EC) in the conductive sample, which produces a secondary magnetic flux in an opposing direction and alternates the input impedance of the excitation coil and receiving probe. Therefore, defects in the sample can be detected since they perturbs the EC and results in variation of the impedance. There are mainly two types of excitation mechanisms for ECT, which are AC eddy current signal [24]–[28] and pulse eddy current (PEC) signal [29]. There are three major types of probing techniques, coil probe [24], [25], giant magneto-resistance (GMR) probe [26]–[28], and the hall sensor [29]. In general, the ECT does not have enough spatial resolution to distinguish errors on different pins of an IC package for example and is not suitable for complex structures such as PCBAs.

In this paper, a compact high-resolution resonance-based capacitive sensor is proposed to detect the defects on the PCBAs, i.e. the shorts and opens. The structure of the sensor can be modeled as a simple LC resonant tank, with a resonant frequency dependent on the sensor trace design and inductance connected to the sensor structure. The simplistic design of the sensor eliminates the need of complex matching circuits design, which makes it easy to fabricate with low cost. Sensor parameters are designed to make the sensor compact and able to detect defects with sufficient sensitivity and spatial resolution. Moreover, simulation and practical results demonstrate the feasibility of the sensor to detect small open and short defects on DUTs. Finally, detail analysis on the sensing principle for the sensor is illustrated using the equivalent circuits which describes the capacitive coupling between the sensor tip and the DUT.

II. THE PROPOSED SENSOR

Fig. 1 (a) and (b) show 3D view and front view of the proposed resonance-based capacitive sensor, respectively. It consists of a capacitive sensing tip (at the bottom, with a zoomed-in view in the insert on the right of Fig. 1 (a)), lumped inductors (at the top), and a connection region that links them (with a zoomed-in view in the insert on the left of Fig. 1 (a)). On top of the inductors, there are input points where signals are fed to the sensor through, e.g. an SMA connector. For the proposed sensor, sensing is obtained by measuring the shift of the resonant frequency which is caused by an interaction between the DUT and the E-field of the capacitive sensing tip, that alters the capacitance of the tip, as shown by the side-view in Fig. 1 (c).

For the proposed structure, the resonant frequency, f_r, is expressed as follows,

$$f_r = \frac{1}{2\pi\sqrt{L_s C_s}} \tag{1}$$

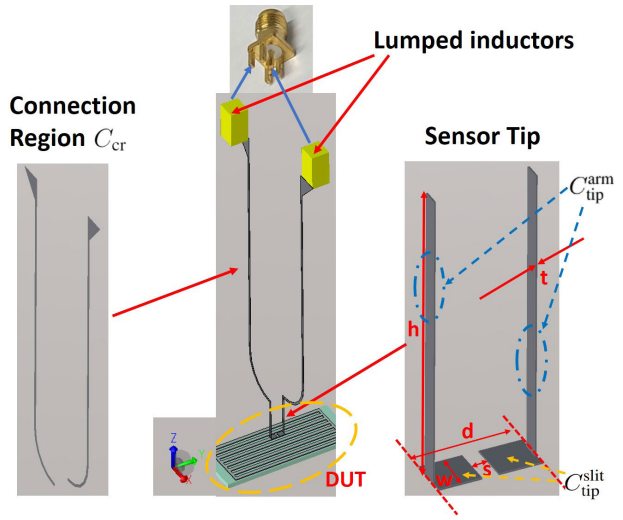

(a) 3D view of the sensor structure.

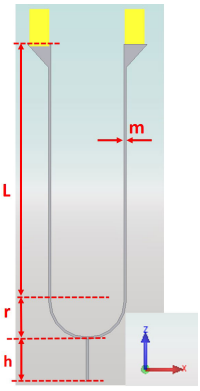

(b) Front view of sensor structure.

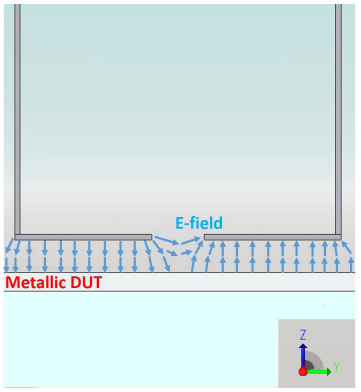

(c) Side view of sensor structure.

FIGURE 1. Overview of the sensor structure.

where

$$C_s = C_{cr} + C_{tip} \tag{2}$$

$$C_{tip} = C_{tip}^{arm} + C_{tip}^{slit} \tag{3}$$

and L_s is the total inductance of the sensor, C_s is the total capacitance of the sensor which is the sum of C_{cr} and C_{tip}, the capacitance contributed by the connection region and that by the sensing tip, respectively. The capacitance from the tip, C_{tip}, has the contribution from the two face-to-face arms, C_{tip}^{arm}, and that from the capacitor in a slit, C_{tip}^{slit} as illustrated in Fig. 1 (a).

For sensing, the shift of the resonance frequency (denoted as Δf_r) is used. When the DUT is underneath the sensing tip, it causes a change in the capacitance of the tip, ΔC_{tip}. Based on Eq. (1)-(3), Δf_r can be expressed using ΔC_{tip} as follows,

$$\Delta f_r = f_r \frac{\sqrt{C_s} - \sqrt{C_s + \Delta C_{tip}}}{\sqrt{C_s + \Delta C_{tip}}} \tag{4}$$

When the sensor is placed above a metal surface, the electric field is disturbed and there is additional capacitive coupling, resulting in an increase in the capacitance of the sensor, i.e. $\Delta C_{tip} > 0$, and thus a downward shifting of the resonant frequency, i.e. $\Delta f_r < 0$, based on Eq. (4).

Upon Eq. (4), the sensitivity for the proposed sensor, denoted as K, is defined as follows,

$$K = \left|\frac{\Delta f_r}{f_r}\right| = \begin{cases} 1 - \sqrt{\dfrac{1}{1 + \Delta C_{tip}/C_s}}, & \text{if } \Delta C_{tip} > 0 \\ \sqrt{\dfrac{1}{1 + \Delta C_{tip}/C_s}} - 1, & \text{otherwise} \end{cases} \tag{5}$$

As shown in Eq. (5), a small intrinsic capacitance of the sensor, C_s, leads to a high sensitivity of the sensor. Therefore, to achieve a high sensitivity, it is preferable to keep the intrinsic C_s low where $C_s = C_{cr} + C_{tip}^{arm} + C_{tip}^{slit}$ according to Eq. (2) and (3). To have a low C_{cr}, in the connection region, the arms are moved apart in the x-direction by introducing a 90^o arch with a radius of r, as shown in Fig. 1 (b). To obtain a small C_{cr}, r is set to be 1.6 mm in this design. After the arch, each arm has a straight section with a length of L before it is connected to the lumped inductors. The length of $L + r$ is decided to be long enough to mitigate the interference of the DUT to the inductors. Thus L is set to 8.4 mm. Besides, the sensor arms have a width of m and a thickness of t. m and t are set to 0.1 mm and 0.01 mm to reduce the C_{cr} and C_{tip}^{arm} with the considerations of the manufacturing capability and cost for the flexible PCB used to produce the sensor.

For the sensing tip, it is designed to have a small physical size in order to have a high spatial sensing resolution to match that of a PCBA, i.e. about 0.15 mm. As shown in Figs. 1 (a) and (b), it has a length of h, an arm-to-arm distance of d, and width of w, and a slit size of s. They are set to 1.8 mm, 0.6 mm, 0.25 mm, and 0.1 mm, respectively. It should be noted that the width of the tip w should be large the guarantee the sensitivity. Meanwhile, it should be small enough to maintain a spatial resolution and to minimize interference from the surrounding of the object under sense. For the slit size s, it need to be kept small to confine the E-field between the sensor slit and guide the E-field pointing to the DUT. In addition, h is chosen to be 1.8 mm to avoid the coupling from the connection region to the DUT since the E-field generated from the connection region spreads broadly in a large area and is not concentrated. To have a compact size, d is preferred to be small. But a small d leads to a high C_{cr} and C_{tip}^{arm}, which leads to a reduction in sensitivity. Therefore, d is decided to be 0.6 mm based the considerations on the physical size and sensitivity. The dimensions of the proposed sensor are tabulated in Table 1.

III. EVALUATION OF THE SENSITIVITY

A. THE DUT

Fig. 2 shows the DUT designed for the evaluation of the proposed sensor. This design is to mimic the metallic traces on PCBAs such as the parallel soldering joints of a chip package, surface mount capacitors or resistors. It is composed

TABLE 1. Optimized parameters of the sensor.

Parameter	h	d	w	s
Dimensions (mm)	1.8	0.6	0.25	0.1
Parameter	L	r	m	t
Dimensions (mm)	8.4	1.6	0.1	0.01

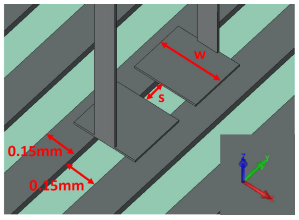

(a) 3D view of the DUT and the sensor.

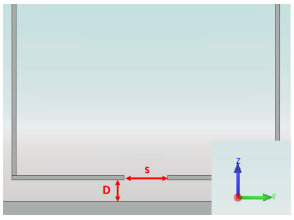

(b) Side view of the DUT and the sensor.

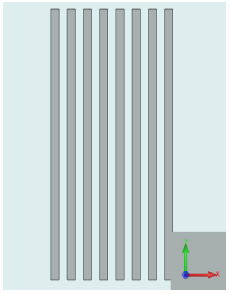

(c) Open termination DUT.

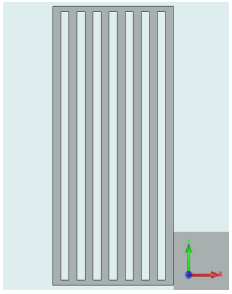

(d) Short termination DUT.

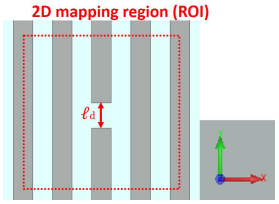

(e) Open defect.

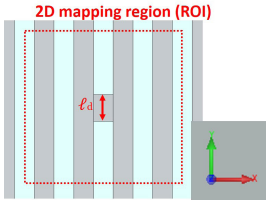

(f) Short defect.

FIGURE 2. Sensor position and creation of DUT traces.

of periodic parallel metallic traces with a width and a spacing both set to 0.15 mm, a thickness of 0.035 mm, and a length of 5 mm, which is of a similar scale of the soldering joints of small outline package (SOP) and quad flat package (QFP) with smallest pitch size [5]. Fig. 2 (a) and (b) show a 3D view and side view of the DUT with the proposed sensor on top of it with a distance of D.

For the termination of the traces, both open and short are included in this study. They are shown in Fig. 2 (c) and (d), respectively. Typically, the terminals of DUT traces can be treated as open to each other. However, in the conditions such as several pins of a chip are linked to the same PCB ground or they are connected inside the die, their terminals can be treated as short to each other. Fig. 2 (e) and (f) show the scenarios when there is an open and a short defect on the DUT in this study, respectively. The length of the defect is ℓ_d. It is set to 0.2 mm which mimics a common defect in a PCBA.

B. NUMERICAL STUDIES

Simulations of the proposed sensor swept on a plane of D above the DUT ($D = 0.05$ mm) were conducted using Keysight EMPro 3D EM Simulation Software. Fig. 2 (a) and (b) show the 3D view and side view of the models. The sweeping regions of interest (ROI) on the xy-plane are indicated by the red dashed boxes in Fig. 2 (e) and (f). They are 1.2 mm × 1.2 mm. The sweeping step sizes in both the x- and the y-direction are set to be 0.075 mm, which is half of the width of the trace or that of the gap. With the dimensions of the sensing tip that were decided by the required sensing spatial resolution, L_s was set to be 0.4 μH where two inductors with an inductance of 0.2 μH each are needed. They are commonly available in the lab. The resultant resonant frequency is 530 MHz which still falls into the region of less than 1 GHz where the supporting accessories are relatively low cost.

Fig. 3 shows the 2D plots of normalized f_r in the ROI. The f_r values are normalized to 528.74 MHz. Fig. 3 (a) and (d) are the plots of the reference mesh without a defect in the frequency range of 528.74 MHz - 529.86 MHz (normalized values of 1.0000 - 1.0021) and 528.43 MHz - 529 MHz (normalized values of 0.9994 - 1.0005), respectively. The former is a reference for the case with an open defect, and the latter is a reference for the case with a short defect. As can be seen in both figures, f_r is relatively low when the sensing tip is above the metal trace whereas it is high when the sensing tip is above the air gap, which is agreeable with the analysis based on Eq. (4) in the previous section. In Fig. 3, only the cases when the DUT is terminated with open ends (shown in Fig. 2 (c)) are shown for the reference conditions because the effect of termination is minor and the cases when the DUT is shorted (shown in Fig. 2 (d)) show similar f_r distribution as those shown in Fig. 3 (a) and (d).

When there is an open or short defect, the 2D f_r distributions are distorted dramatically with distinguishable patterns. Fig. 3 (b) and (e) show the plots when there is an open and a short defect in the situation when the DUT are terminated with opens, respectively, whereas Fig. 3 (c) and (f) show those in the situation when the traces of the DUT are shorted. The locations of the metallic traces are indicated by the gray dashed boxes in the figures.

As shown in Fig. 3 (b) and (c), when there is an open defect at the center of ROI, compared with the reference in Fig. 3 (a), it is found that f_r increases around the defect which is due to a decrease in the capacitance near the sensor tip based on Eq. (4). It forms a distinguishable bright pattern for detection.

When the traces are shorted, as shown in Fig. 3 (c), a distinguishable pattern is still seen with a relatively small increase in f_r.

Meanwhile, a short defect also shows a distinguishable pattern in the f_r distributions, as shown in Fig. 3 (e) and (f) for the cases when the traces are open and short, respectively. With a metallic block introduced between the two traces to mimic a short defect, the region around the defect has a decrease in f_r forming a dark pattern for detection. The

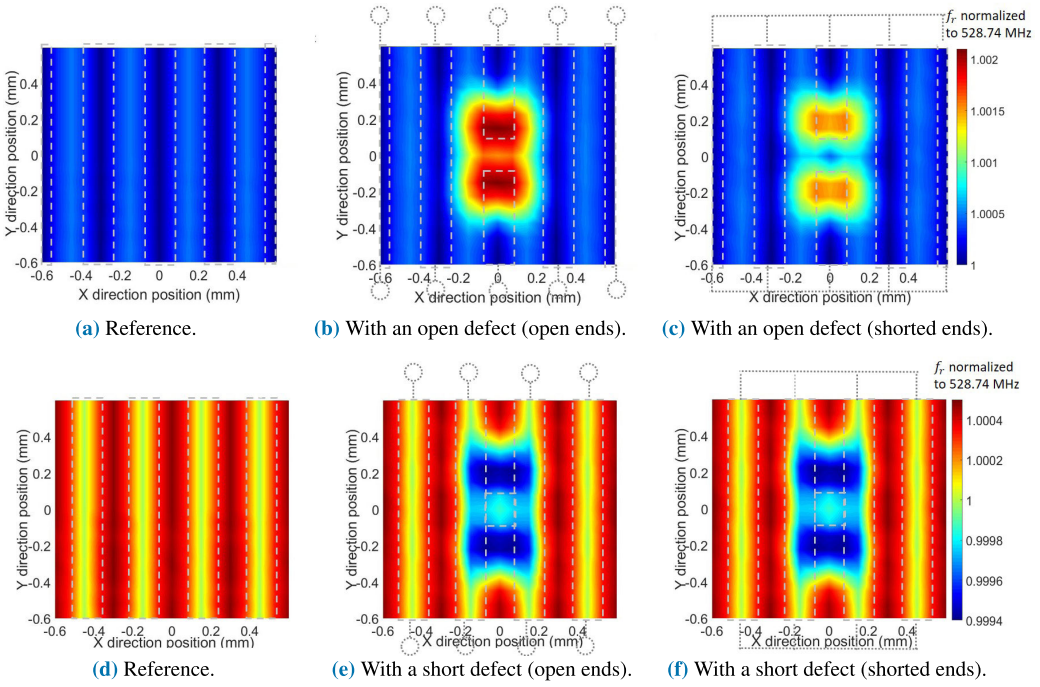

(a) Reference. (b) With an open defect (open ends). (c) With an open defect (shorted ends).

(d) Reference. (e) With a short defect (open ends). (f) With a short defect (shorted ends).

FIGURE 3. Simulated f_r distributions of the DUT with open and short defects.

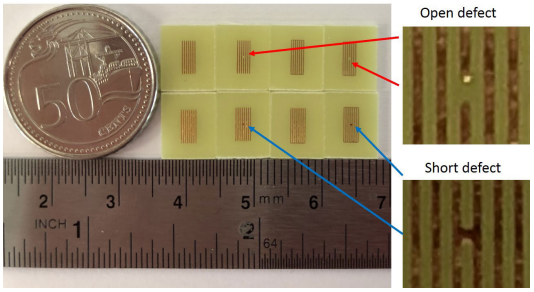

FIGURE 4. Sample DUT with open and short defects on it.

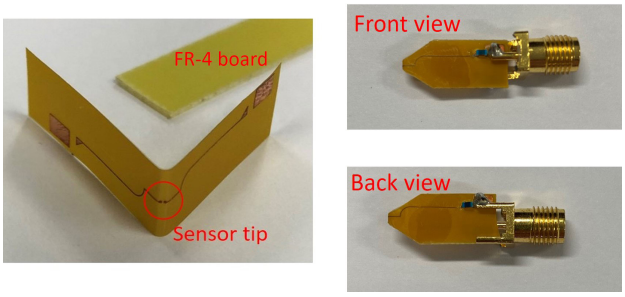

(a) Flexible PCB and FR-4 board used for sensor fabrication. (b) Front and back views of the fabricated sensor.

FIGURE 5. Practical sensor fabrication.

decreased f_r is due to an increase in the capacitance near the sensor tip based on Eq. (4). For both types of defects, a detailed circuit analysis on the interaction of the sensor tip and the DUT traces will be presented in Section IV.

C. EXPERIMENTAL VALIDATIONS

Both the proposed sensor and the DUTs were fabricated for experimental validations. Fig. 4 shows a photo of the DUT with open and short defects. Flexible PCB was used for the fabrication of the proposed sensor, the metallic traces of the sensor was etched from flexible copper clad laminate (FCCL) (the FCCL is from Hubei Hengchi Electronic Technology Co., Ltd). And the polyethylene terephthalate (PET) layer and copper layer of the FCCL have a thickness of around 0.02 mm and 0.01 mm, respectively. Then the fabricated flexible PCB was folded and pasted on a FR-4 board (with a thickness of 0.6 mm), as shown in Fig. 5 (a). Fig. 5 (b) shows the photos of the front and back view of the built sensor with a SMA connector soldered to facilitate a connection to a vector network analyzer (VNA) for a measurement. The sensor was characterized by measuring the S_{11} using a VNA (N5249B, Keysight Technologies) over a frequency range from 530 MHz to 550 MHz with 1001 sampling points in between. Fig. 6 shows the S_{11} versus the frequency. As shown in Fig. 6, the sensor resonates at around 540.24 MHz with good matching (i.e. a $|S_{11}|$ of around -38 dB).

The experimental validations for the detection of defects were conducted by sweeping the DUT within the same ROI as the simulations using the sensor when it was placed vertically 0.05 mm above the DUT. Fig. 7 shows the experimental setup of the measurement which consists of the positioning platform (VT-80 linear stage, Physik Instrumente) that can precisely controls the movement of the sensor (a minimum step size of 1 um) in the x-, y-, and z-direction and a VNA (N5249B, Keysight Technologies). The sensor was moved with respect to the DUT to cover the ROI and the S_{11}'s

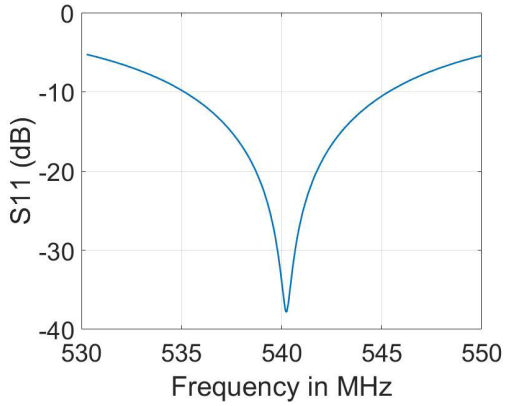

FIGURE 6. Practical sensor results without DUT.

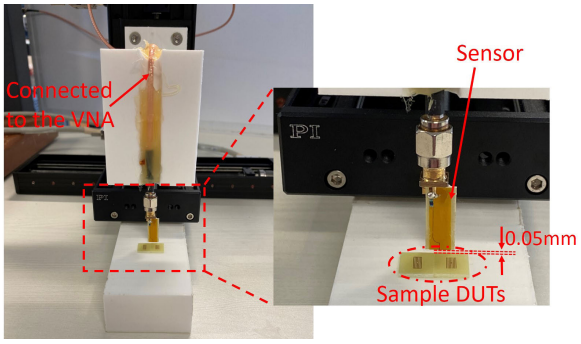

FIGURE 7. Experimental setup.

over the frequency range from 530 MHz to 550 MHz (with 1001 sampling points in between) were recorded.

Fig. 8 shows the normalized measured f_r distributions of the fabricated samples when there was an open or a short defect. Comparing the measured results in Fig. 8 to the simulated ones in Fig. 3, they agree well with each other in each case. It is noted that the frequencies that f_r is normalized to have slightly difference between simulation and practical results, and it is mainly due to the discrepancy of L_s and C_s value in practical fabrication. The agreements strongly imply detection of either open or short are practically possible by using the proposed sensor design.

IV. DISCUSSION

The detection of open or short in a group of parallel metallic traces is accomplished through a distinguishable pattern in the f_r distribution in a 2D scan using the proposed sensor tip. In both Fig. 3 and Fig. 8, it is observed that the pattern is slightly larger than the defect, and different terminations of the traces may result in difference in f_r. In this section, circuit models of the sensor tip with the DUT are proposed to explain the observations, and to provide further insights to the sensor design.

The equivalent circuit of the sensor is shown in Fig. 9 (a), where L_s and R_s are the equivalent inductance and resistance of the sensor besides the capacitance, C_{cr} and C_{tip} that were introduced previously, R_{vna} is the output impedance of the VNA that equals to 50 ohms, and E_1 is the signal source from the VNA. When the sensor tip is placed near the DUT, additional capacitive coupling is induced between the sensor tip and the DUT (with and without defects), thus more detailed circuit models are proposed for different situations which are used to replace C_{tip}.

A. OPEN DEFECT CASE

Fig. 9 (b) and (c) show the detailed circuit model in the situation when the proposed sensor is placed on top of a trace of DUT (i.e. the reference case for open defect) and in the situation when there is a open defect, respectively. These two situations with the capacitive coupling between the sensor tip and the DUT are shown in Fig. 9 (d) and (e), respectively. Fig. 9 (f) shows a side view of Fig. 9 (e).

Fig. 9 (b) shows the proposed configuration of the coupling capacitance for the reference case for open defect, $C^{\text{o-ref}}_{\text{B-B}}$, $C^{\text{o-ref}}_{\text{Bi-t}}$, $C^{\text{o-ref}}_{\text{Bi-St}}$ ($i = 1,2$), and Fig. 9 (d) illustrates the source of the coupling in the setup. The superscript, o-ref, stands for open reference, the subscript B, t, St, and i, denote the correspondence to branch, trace, surrounding trances, and the i^{th} branch arm, respectively. As shown in Fig. 9 (d), $C^{\text{o-ref}}_{\text{B-B}}$, $C^{\text{o-ref}}_{\text{Bi-t}}$, $C^{\text{o-ref}}_{\text{Bi-St}}$ ($i = 1,2$) are the capacitance between the two branches of the sensor tip, that between the i^{th} branch and the trace underneath (labelled with trace), and that between the i^{th} branch and all the other surrounding DUT traces except the one underneath the sensor. $C^{\text{o-ref}}_{\text{B-B}}$ and $C^{\text{o-ref}}_{\text{Bi-St}}$ are referred as peripheral components and $C^{\text{o-ref}}_{\text{Bi-t}}$ referred as central components based on the configuration in Fig. 9 (b).

When there is an open introduced underneath the sensor tip, more coupling capacitance are needed to be considered. When the traces are open, Fig. 9 (c) shows the proposed configurations of the capacitance and Fig. 9 (e) illustrates the source of the coupling in the setup. The superscript, o, is used to represent open defect. Comparing to the reference case, more capacitances are introduced to the central components. As shown, $C^{\text{o}}_{\text{t-t}}$, $C^{\text{o}}_{\text{Bi-ti}}$, and $C^{\text{o}}_{\text{ti-St}}$ ($i = 1,2$) are the new coupling capacitance due to the introduction of an open to the trace which break the trace into two parts, half trace 1 and 2 that are denoted using subscript, t1 and t2. As shown in Fig. 9 (e) and (f), $C^{\text{o}}_{\text{t-t}}$, $C^{\text{o}}_{\text{Bi-ti}}$, and $C^{\text{o}}_{\text{ti-St}}$ are the capacitance between the two half traces, that between the i^{th} branch of sensor tip and the i^{th} half trace, and that between the i^{th} half trace and all the other surrounding traces except the opposite half trace. When the traces are shorted, $C^{\text{o}}_{\text{ti-St}}$ ($i = 1,2$) are shorted.

In order to verify the accuracy of the circuit models, the values of all the capacitance components in the equivalent circuits were extracted (using CST EM Studio) when the sensor tip is at different xy-locations above the DUT (0.05 mm above the DUT) within the ROI when the traces are open. For the circuit when the traces are shorted, $C^{\text{o}}_{\text{ti-St}}$ ($i = 1,2$) are shorted.

With the extracted capacitance value of all the components and equivalent circuits shown in Fig. 9 (b) and (c), f_r can be

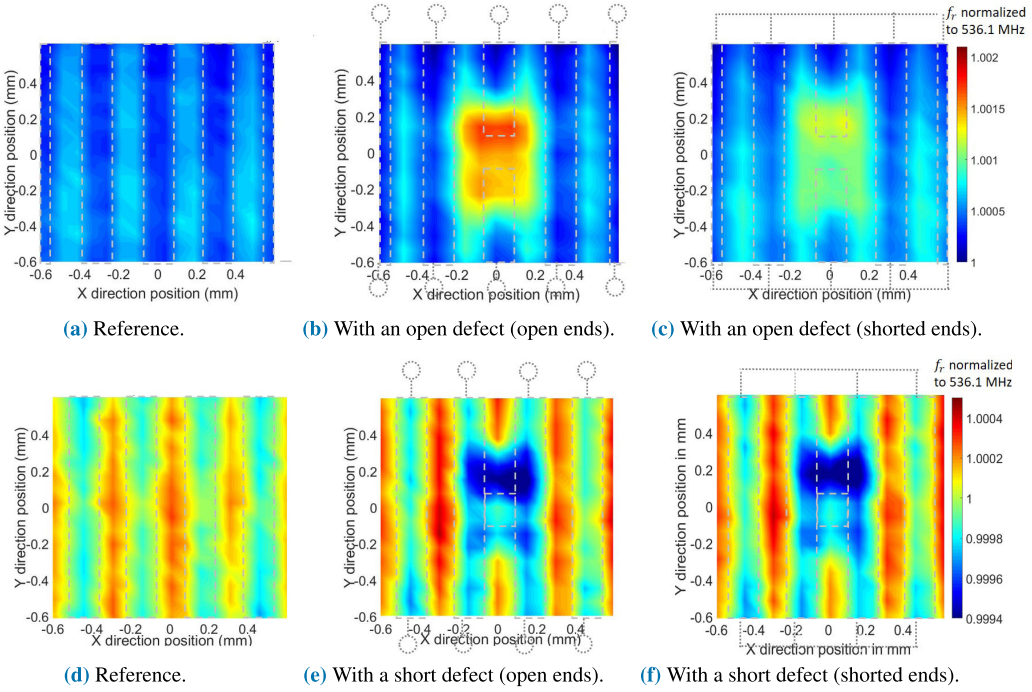

(a) Reference. (b) With an open defect (open ends). (c) With an open defect (shorted ends).

(d) Reference. (e) With a short defect (open ends). (f) With a short defect (shorted ends).

FIGURE 8. Practical f_r distributions of the DUT with open and short defects.

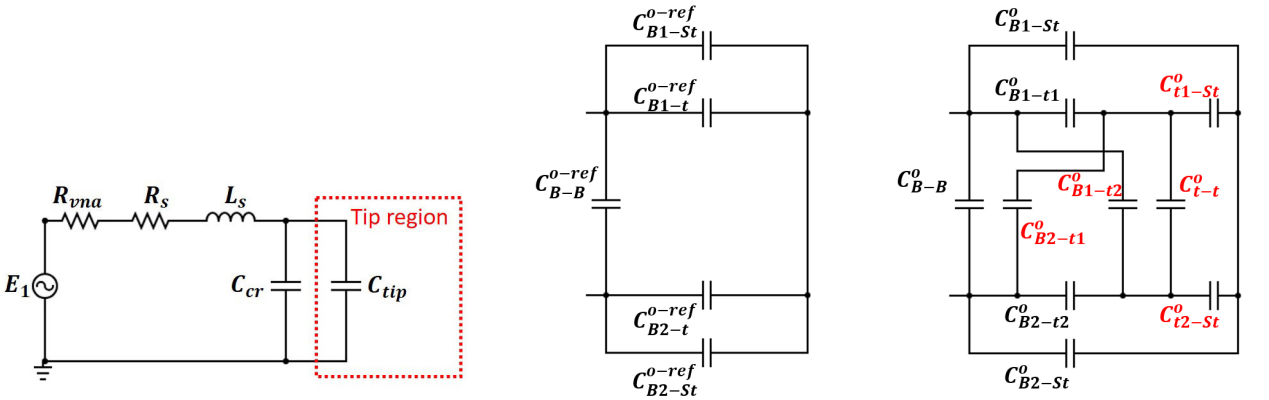

(a) The equivalent circuit for the proposed sensor. (b) The tip region without open defect. (c) The tip region with open defect.

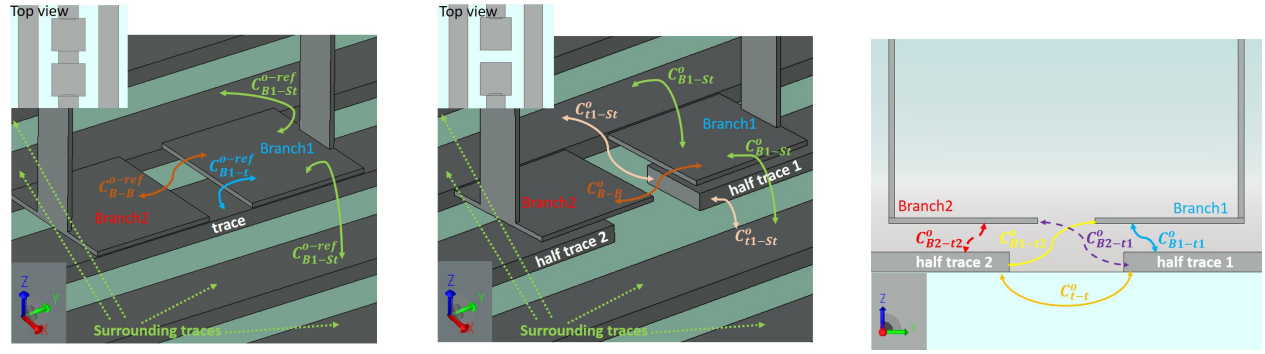

(d) Capacitive coupling for reference without open defect (3D view). (e) Capacitive coupling for open defect condition (3D view). (f) Capacitive coupling for open defect condition (side view).

FIGURE 9. Equivalent circuits and illustrations for capacitive coupling between sensor tip and DUT traces for open defect detection.

calculated based on Eq. (1) and (2). When the f_r calculated from the model is compared with the simulation results as shown in Fig. 3 (a), (b) and (c). the variation was found to be less than 50 ppm in the ROI. Thus, the accuracy of these circuit models is verified.

The 2D plot patterns caused by the open defect as shown in Fig. 3 (b) and (c) are explained with the help of the equivalent circuits. Due to the symmetry of the DUT and sensor in the reference case, $C^{\text{o-ref}}_{\text{B1-t}} = C^{\text{o-ref}}_{\text{B2-t}} = C^{\text{o-ref}}_{\text{B-t}}$, and $C^{\text{o-ref}}_{\text{B1-St}} = C^{\text{o-ref}}_{\text{B2-St}} = C^{\text{o-ref}}_{\text{B-St}}$. To further simplify the analysis, the capacitance components in the open defect condition are normalized to the open reference condition as follows,

$$\begin{aligned} C^{\text{o}}_{\text{B1-t1}} &= k_1 C^{\text{o-ref}}_{\text{B-t}} \\ C^{\text{o}}_{\text{B1-t2}} &= k_2 C^{\text{o-ref}}_{\text{B-t}} \\ C^{\text{o}}_{\text{B2-t1}} &= k_3 C^{\text{o-ref}}_{\text{B-t}} \\ C^{\text{o}}_{\text{B2-t2}} &= k_4 C^{\text{o-ref}}_{\text{B-t}} \\ C^{\text{o}}_{\text{t1-St}} &\approx C^{\text{o}}_{\text{t2-St}} \\ &= C^{\text{o}}_{\text{t-St}} = 2k_5 C^{\text{o-ref}}_{\text{B-t}} \\ (C^{\text{o}}_{\text{B-B}} - C^{\text{o-ref}}_{\text{B-B}}) + 0.5(C^{\text{o}}_{\text{B-St}} - C^{\text{o-ref}}_{\text{B-St}}) &= k_6 C^{\text{o-ref}}_{\text{B-t}} \end{aligned} \tag{6}$$

where $k_i > 0$ $(i = 1,\ldots 6)$, k_5 indicates the coupling between the trace underneath the sensor tip and the surrounding traces, k_6 reflects the change in the peripheral capacitance due to the open defect, and $C^{\text{o}}_{\text{B-St}} = C^{\text{o}}_{\text{B1-St}}$ or $C^{\text{o}}_{\text{B2-St}}$ where $C^{\text{o}}_{\text{B1-St}} \approx C^{\text{o}}_{\text{B2-St}}$. In Eq. (6), owing to the physical configuration between the sensor tip, the DUT, and the open defect, $0 < k_1, k_2, k_3, k_4 < 1, k_1 + k_2 < 1$. When an open defect was introduced, the capacitance between one of the branches to the trace, for example, for branch 1, $C^{\text{o-ref}}_{\text{B1-t}}$ is split into two parts, $C^{\text{o}}_{\text{B1-t1}}$ and $C^{\text{o}}_{\text{B1-t2}}$, and $C^{\text{o-ref}}_{\text{B1-t}} > C^{\text{o}}_{\text{B1-t1}} + C^{\text{o}}_{\text{B1-t2}}$ due to an increase in the distance introduced by the opening, therefore, $k_1 + k_2 < 1$. With the same token, $k_3 + k_4 < 1$. When there are no surrounding traces, $k_5 = 0$.

In Fig. 3 and Fig. 8, f_r is increased dramatically near the open defect, forming a bright patch for the detection. The increase in f_r is caused by a decrease in C_{tip} which is denoted as $\Delta C_{\text{tip-o}}$ where the subscript o indicates an open defect.

Based on the proposed circuits shown in Fig. 9 (b) and (c), and expressions in Eq. (6), $\Delta C_{\text{tip-o}}$ can be approximately expressed as follows,

$$\Delta C_{\text{tip-o}} = C^{\text{o}}_{\text{tip}} - C^{\text{o-ref}}_{\text{tip}} \approx C^{\text{o-ref}}_{\text{B-t}}(M + N + P + k_6 - 0.5) \tag{7}$$

where $M = \frac{k_1 k_3}{k_1 + k_3}$, $N = \frac{k_2 k_4}{k_2 + k_4}$, and P is expressed in Eq. (8) below,

$$P = \frac{k_5(k_1 k_4 - k_2 k_3)^2}{(k_1 + k_3)(k_2 + k_4)} \times \frac{1}{((k_1 + k_3)(k_2 + k_4) + k_5(k_1 + k_2 + k_3 + k_4))} \tag{8}$$

As $\Delta C_{\text{tip-o}} < 0$, $M + N + P + k_6 < 0.5$. Within this range, an increase in $(M + N + P + k_6)$ leads to a decrease in $|\Delta C_{\text{tip-o}}|$ which lower Δf_r. Moreover, M corresponds to the contribution along the path from $C^{\text{o}}_{\text{B1-t1}}$ to $C^{\text{o}}_{\text{B2-t1}}$, and N corresponds to the other one from $C^{\text{o}}_{\text{B1-t2}}$ to $C^{\text{o}}_{\text{B2-t2}}$ in Fig. 9 (c), while P is closely related to the coupling between the trace underneath the sensor tip and the surrounding traces (i.e. k_5). It is noted that when the traces have a higher pitch (i.e. they are far apart), k_5 decreases, and so is P. When the traces are shorted, $C_{\text{ti-St}}$ is replaced by short circuits, and $k_5 \to \infty$, P becomes $P = \frac{(k_1 k_4 - k_2 k_3)^2}{(k_1 + k_3)(k_2 + k_4)(k_1 + k_2 + k_3 + k_4)}$ which is an increase compared to the value in Eq. (8). An increase in P leads to an drop in $|\Delta C_{\text{tip-o}}|$, thus resulting in a lower shift in f_r when the traces are shorted compared to those in the case when they are open. The circuit model helps to explain the size of the bright patch that is used for defect detections. Fig. 10 (a) and (b) show the changes of M, N, P, and k_6 when the sensor tip moves along the y- and the x-direction, respectively. When the sensor tip is moving along the y-direction, $C^{\text{o-ref}}_{\text{B-t}}$ stays constant. In Fig. 10 (a), the horizontal axis y represent the the distance between the center of the tip to that of the open defect along the y-direction. Comparing all the curves, N and k_6 are relatively small and decrease slowly when y increases. P in the case when the traces are shorted (the purple curve) is higher than that in the case when the traces are open (the yellow curve), as explained in the previous paragraph. Moreover, it is observed that P dominates when $y < 0.125$ mm and beyond $y = 0.125$ mm, M dominates. M increases as y increases, which decreases $|\Delta C_{\text{tip-o}}|$ based on Eq. (7) and lowers Δf_r. Therefore, the knee of the slope of M decides the boundary of the patch which is directly related to the resolution of detection. In this case, beyond $y \approx 0.4$ mm, M becomes more than 0.42, $|\Delta C_{\text{tip}}| < 0.1$ fF, and no obvious shift of f_r is observed.

When the sensor tip is moving along the x-direction, $C^{\text{o-ref}}_{\text{B-t}}$ varies. In Fig. 10 (b), due to the symmetry with respect to the x-axis, N = M, thus 2M is plotted. Besides, it shows the variation of P, k_6, and $C^{\text{o-ref}}_{\text{B-t}}$ with respect to x where x is defined as the distance between the center of the tip to that of the open defect along the x-direction. For the reference capacitance, $C^{\text{o-ref}}_{\text{B-t}}$ decays as x increases. Comparing the curves for 2M, P, and k_6, similar to the case along the y-direction, k_6 are relatively small and decrease slowly when y increases, and P in the case when the traces are shorted is higher than that in the case when the traces are open. Both P curves decays as x increases whereas the curve for 2M

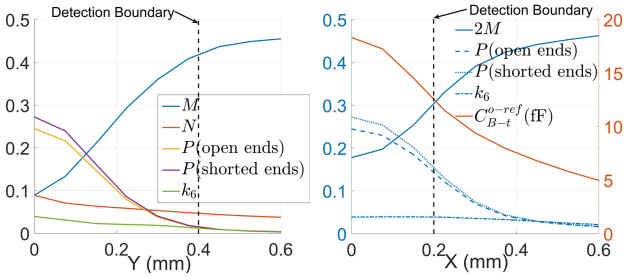

(a) Positive Y direction sweep. **(b)** Positive X direction sweep.

FIGURE 10. Sensor tip sweeping investigations for open defect detection.

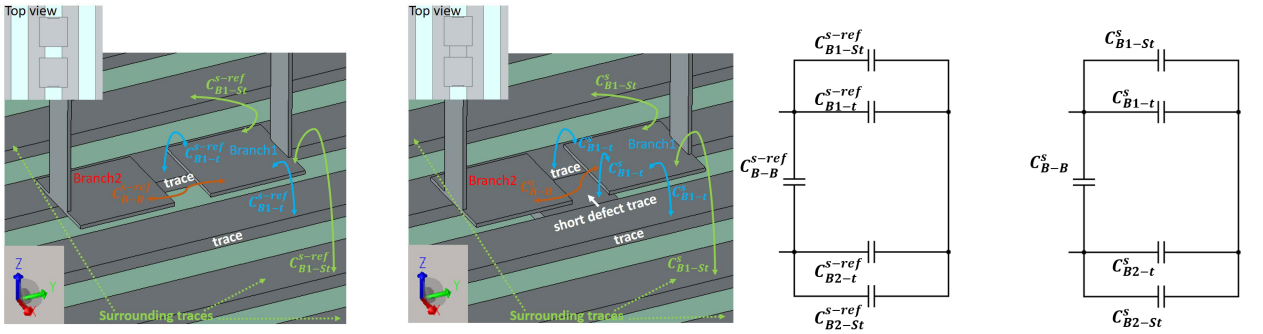

(a) Capacitive coupling for reference without short defect.

(b) Capacitive coupling with short defect.

(c) The tip region without short defect.

(d) The tip region with short defect.

FIGURE 11. Equivalent circuits and illustrations for capacitive coupling between sensor tip and DUT traces for short defect detection.

increases. At point $x \approx 0.2$ mm and beyond, $|\Delta C_{\text{tip}}| < 0.1$ fF and no obvious shift of f_r is observed. It decides the boundary of the patch along this direction.

B. SHORT DEFECT CASE

A short defect most likely happens in between two traces. Therefore, for the case with a short defect, the reference case has the sensor tip is placed above the gap between two traces, as shown in Fig. 11 (a). When there is a short introduced underneath the sensor tip, unlike the case with an open defect where more coupling capacitance are needed to be considered, the coupling capacitance stays a similar configuration as that of the reference case. Fig. 11 (c) and (d) show the circuit model of the reference case and that with a short defect, respectively. Fig. 11 (a) and (b) illustrate the source of the coupling in the setup. The superscript, s, is used to represent short defect. The rest of the content in the superscript and the subscript have the similar meaning as the open defect case in the setup. Similarly, the capacitance in Fig. 11 (d) can be expressed based on those in the reference case. They are shown as follows,

$$\begin{aligned} C^{\text{s}}_{\text{B1-t}} &= k_7 C^{\text{s-ref}}_{\text{B-t}} \\ C^{\text{s}}_{\text{B2-t}} &= k_8 C^{\text{s-ref}}_{\text{B-t}} \\ (C^{\text{s}}_{\text{B-B}} - C^{\text{s-ref}}_{\text{B-B}}) + 0.5(C^{\text{s}}_{\text{B-St}} - C^{\text{s-ref}}_{\text{B-St}}) &= k_9 C^{\text{s-ref}}_{\text{B-t}} \end{aligned} \quad (9)$$

where $k_7, k_8 > 1, k_9 < 0$.

For a short defect, in Fig. 3 and Fig. 8, f_r is increased dramatically near the short defect, forming a dark patch for the detection. The decrease in f_r is caused by an increase in C_{tip}, $\Delta C_{\text{tip-s}}$, where the subscript s indicates a short defect.

Based on the proposed circuits shown in Fig. 11 (c) and (d), and expressions in Eq. (9), $\Delta C_{\text{tip-s}}$ can be approximately expressed as follows,

$$\Delta C_{\text{tips}} \approx C^{\text{s-ref}}_{\text{B1-t}}(Q + k_9 - 0.5) > 0 \quad (10)$$

where

$$Q = \frac{k_7 k_8}{k_7 + k_8} > 0.5 \quad (11)$$

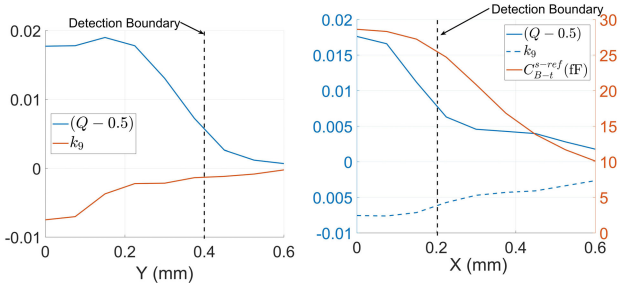

(a) Positive Y direction sweep.

(b) Positive X direction sweep.

FIGURE 12. Sensor tip sweeping investigations for short defect detection.

Next, the circuit model in Figs. 11 (c) and (d) helps to explain the size of the dark patch for the short defect detection. Figs. 12 (a) and (b) show the changes of $(Q-0.5)$ and k_9 when the sensor tip moves along the y- and the x-direction, respectively. When the sensor tip is moving along the y-direction, $C^{\text{s-ref}}_{\text{B-t}}$ stays constant. In Fig. 10 (a), comparing all the curves, $(Q-0.5)$ starts to decrease rapidly at $y \approx 0.2$ mm, and becomes steady at the location of $y \approx 0.4$ mm, which determines the boundary of the patch. While k_9 becomes steady when $y > 0.2$ mm, which has small effect on the patch boundary.

When the sensor tip is moving along the x-direction, $C^{\text{s-ref}}_{\text{B-t}}$ varies. As shown in Fig. 12 (b), it is noted that $(Q - 0.5)$ dramatically decreases at the range of $x < 0.2$ mm, however, $C^{\text{s-ref}}_{\text{B-t}}$ and k_9 almost remain constant in this range, therefore, Q is still the major parameter that determines the boundary of the patch along x direction.

C. COMPARISON TO THE EXISTING SOLUTIONS

For the existing E-field-based near-field RF NDE methods in the literature, for the methods using open-ended coaxial probing technique [14]–[17], the spatial resolution lies in the range from a few millimetres to a few centimetres, which is relatively large. While for the methods using cavity resonance technique [18], [19], SRRs [13], [20], [21], and open-ended waveguide slit [22], [23], the spatial resolution could be high but the cost will increase due to higher working frequency,

complex fabrication process or measurement setup. For the H-field-based RF NDE methods mentioned in [24]–[29], recent progresses from [26], [28] could detect single thin crack with width equals to 0.1 mm on a bare metal plate, but the sensor size falls in the range of more than a few millimeters, which means the spatial resolution is not enough to distinguish errors in the complex PCBA environment. Comparing the imaging performance of the proposed sensor with the existing near-field RF NDE methods in the literature, it can be found that the proposed sensor has sufficient spatial resolution to distinguish the open and short defects on different pins of an IC package. And the simple fabrication process and relatively low operating frequency reduce the overall cost.

V. CONCLUSION

This paper presents a compact near-field split resonator sensor for open and short defects detection on modern PCBAs. The sensor structure has been designed that strong electric field is confined at the sensor tip for defects sensing. Moreover, the sensitivity of the sensor is verified using both simulation and practical results. Therefore, the proposed sensor shows great potential for microwave imaging setup to detect defects on PCBAs in the manufacturing supply chain. Besides, detail circuit models have been made to explain the detection principle and boundary, and it helps explain how the DUT traces termination types will influence the sensitivity of the sensor. Future work involves the integration of the sensor in a sensing array that will accelerate the measurement speed.

REFERENCES

[1] J. E. Monagas Martin, A. S. Nevado, and A. V. Martinez, "Low cost programmable modular system to perform in-circuit test (ICT) full development of the hardware, software and mechanics of an ICT machine," in *Proc. Technol. Appl. Electron. Teaching (TAEE)*, Jun. 2016, pp. 1–7.

[2] A. J. Albee, "The evolution of ICT: PCB technologies, test philosophies, and manufacturing business models are driving in-circuit test evolution and innovations," in *Proc. Conf. Exhib. (IPC APEX EXPO)*, vol. 1, 2013, pp. 381–401.

[3] M. R. Johnson, "The increasing importance of utilizing non-intrusive board test technologies for printed circuit board defect coverage," in *Proc. IEEE AUTOTESTCON*, Sep. 2018, pp. 1–5.

[4] M. Serban, Y. Vagapov, Z. Chen, R. Holme, and S. Lupin, "Universal platform for PCB functional testing," in *Proc. Int. Conf. Actual Problems Electron Devices Eng. (APEDE)*, vol. 2, Sep. 2014, pp. 402–409.

[5] X. Ma, B. Xu, Y. Cheng, F. Liu, Z. Liang, B. Chen, S. Li, H. Mo, Z. Zhong, and H. Wang, "Flexible connection for reflow free fine pitch SMT components," in *Proc. 18th Int. Conf. Electron. Packag. Technol. (ICEPT)*, Aug. 2017, pp. 575–579.

[6] M. Oppermann, T. Zerna, and K.-J. Wolter, "X-ray computed tomography for nano packaging—A progressive NDE method," in *Proc. 12th Electron. Package. Technol. Conf.*, Dec. 2010, pp. 853–858.

[7] A. Liu, C. Zou, T. Lin, J. Li, C. K. Tan, Z. J. Feng, D. Geiger, S. Liu, J. P. Wen, J. Xiao, L. Liu, and E. Krastev, "X-ray inspection methods for controlling PCBA potting process—2DX and partial angle computer tomography," in *Proc. Pan Pacific Microelectron. Symp. (Pan Pacific)*, Jan. 2016, pp. 1–5.

[8] N. E. B. Alaoui, A. Cassou, P. Tounsi, A. Boyer, and A. Viard, "Using infrared thermal responses for PCBA production tests: Feasibility study," *Microelectron. Rel.*, vols. 100–101, Sep. 2019, Art. no. 113354.

[9] A. Stoynova, B. Bonev, and N. Brayanov, "Thermographic approach for reliability estimation of PCB," in *Proc. 41st Int. Spring Seminar Electron. Technol. (ISSE)*, May 2018, pp. 1–7.

[10] M. Abbas and M. Shafiee, "Structural health monitoring (SHM) and determination of surface defects in large metallic structures using ultrasonic guided waves," *Sensors*, vol. 18, no. 11, p. 3958, Nov. 2018.

[11] G. Chang, M. Chen, D. Lee, J. Lee, G. Ramakrishna, J. Oliver, and T. Chou, "A new detection method for the onset of PCB pad cratering," in *Proc. 8th Int. Microsyst., Packag., Assem. Circuits Technol. Conf. (IMPACT)*, Oct. 2013, pp. 96–100.

[12] D. Kumar, S. Karuppuswami, Y. Deng, and P. Chahal, "A wireless shortwave near-field probe for monitoring structural integrity of dielectric composites and polymers," *NDT E Int.*, vol. 96, pp. 9–17, Jun. 2018.

[13] S. Mukherjee, X. Shi, L. Udpa, S. Udpa, Y. Deng, and P. Chahal, "Design of a split-ring resonator sensor for near-field microwave imaging," *IEEE Sensors J.*, vol. 18, no. 17, pp. 7066–7076, Sep. 2018.

[14] D. Popovic, L. McCartney, C. Beasley, M. Lazebnik, M. Okoniewski, S. C. Hagness, and J. H. Booske, "Precision open-ended coaxial probes for *in vivo* and ex vivo dielectric spectroscopy of biological tissues at microwave frequencies," *IEEE Trans. Microw. Theory Techn.*, vol. 53, no. 5, pp. 1713–1722, May 2005.

[15] D. V. Blackham and R. D. Pollard, "An improved technique for permittivity measurements using a coaxial probe," *IEEE Trans. Instrum. Meas.*, vol. 46, no. 5, pp. 1093–1099, Oct. 1997.

[16] A. P. O'Rourke, M. Lazebnik, J. M. Bertram, M. C. Converse, S. C. Hagness, J. G. Webster, and D. M. Mahvi, "Dielectric properties of human normal, malignant and cirrhotic liver tissue: *In vivo* and *ex vivo* measurements from 0.5 to 20 GHz using a precision open-ended coaxial probe," *Phys. Med. Biol.*, vol. 52, no. 15, pp. 4707–4719, Aug. 2007.

[17] D. M. Hagl, D. Popovic, S. C. Hagness, J. H. Booske, and M. Okoniewski, "Sensing volume of open-ended coaxial probes for dielectric characterization of breast tissue at microwave frequencies," *IEEE Trans. Microw. Theory Techn.*, vol. 51, no. 4, pp. 1194–1206, Apr. 2003.

[18] A. P. Gregory, J. F. Blackburn, K. Lees, R. N. Clarke, T. E. Hodgetts, S. M. Hanham, and N. Klein, "A near-field scanning microwave microscope for measurement of the permittivity and loss of high-loss materials," in *Proc. 84th ARFTG Microw. Meas. Conf.*, Dec. 2014, pp. 1–8.

[19] D. E. Steinhauer, C. P. Vlahcos, F. C. Wellstood, S. M. Anlage, C. Canedy, R. A. Ramesh amd Stanishevsky, and J. Melng, "Quantitative imaging of dielectric permittivity and tunability with a near-field scanning microwave microscope," *Rev. Sci. Instrum.*, vol. 71, p. 2751, Jul. 2000.

[20] D. Isakov, C. J. Stevens, F. Castles, and P. S. Grant, "A split ring resonator dielectric probe for near-field dielectric imaging," *Sci. Rep.*, vol. 7, no. 1, p. 2038, May 2017.

[21] N. Wiwatcharagoses, K. Y. Park, and P. Chahal, "Metamaterial-inspired miniaturized microwave sensing probes," in *Proc. IEEE 62nd Electron. Compon. Technol. Conf.*, May 2012, pp. 2106–2111.

[22] M. Abu-Teir, M. Golosovsky, D. Davidov, A. Frenkel, and H. Goldberger, "Near-field scanning microwave probe based on a dielectric resonator," *Rev. Sci. Instrum.*, vol. 72, no. 4, pp. 2073–2079, Apr. 2001.

[23] M. Golosovsky and D. Davidov, "Novel millimeter-wave near-field resistivity microscope," *Appl. Phys. Lett.*, vol. 68, no. 11, pp. 1579–1581, Mar. 1996.

[24] S. Soeung, N. B. Zain Ali, M. H. Md Khir, and A. Ahmadi, "Printed circuit board fault inspection based on eddy current testing using planar coil sensor," *Modern Appl. Sci.*, vol. 8, no. 2, p. 142, Mar. 2014.

[25] K. H. Lee, M. K. Baek, and I. H. Park, "Estimation of deep defect in ferromagnetic material by low frequency eddy current method," *IEEE Trans. Magn.*, vol. 48, no. 11, pp. 3965–3968, Nov. 2012.

[26] A. Bernieri, L. Ferrigno, M. Laracca, and A. Rasile, "Eddy current testing probe based on double-coil excitation and GMR sensor," *IEEE Trans. Instrum. Meas.*, vol. 68, no. 5, pp. 1533–1542, May 2019.

[27] D. Rifai, A. Abdalla, R. Razali, K. Ali, and M. Faraj, "An eddy current testing platform system for pipe defect inspection based on an optimized eddy current technique probe design," *Sensors*, vol. 17, no. 3, p. 579, Mar. 2017.

[28] G. D'Angelo, M. Laracca, S. Rampone, and G. Betta, "Fast eddy current testing defect classification using Lissajous figures," *IEEE Trans. Instrum. Meas.*, vol. 67, no. 4, pp. 821–830, Apr. 2018.

[29] J. Wu, D. Zhou, J. Wang, X. Guo, L. You, W. An, and H. Zhang, "Surface crack detection for carbon fiber reinforced plastic (CFRP) materials using pulsed eddy current testing," in *Proc. IEEE Far East Forum Nondestruct. Eval./Test.*, Jun. 2014, pp. 181–185.

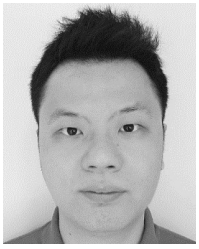

TIE QIU (Member, IEEE) received the B.Eng. degree from Nanyang Technological University, Singapore, in 2014. He is currently pursuing the Ph.D. degree with the Pillar of Engineering Product Development, Singapore University of Technology and Design (SUTD), Singapore. He was a System Engineer with Rohde & Schwarz, Singapore, from 2014 to 2018. He has been with Keysight Technologies, Singapore, as a Research and Development Engineer, since 2018. His research interests include industrial electronics, microwave theory and techniques, and electronic test and measurements.

CHOON KAIT ANDREW TEK received the M.Sc. degree in electronics from Queen's University Belfast, U.K. He held different roles in application engineering, product marketing, and strategic procurement. He is currently a Strategic Planner with Keysight Technologies. His research interests include electronic test and measurement and manufacturing test technologies.

SHAO YING HUANG (Member, IEEE) received the B.Eng., M.Eng., and Ph.D. degrees from Nanyang Technological University, Singapore, in 2003, 2006, and 2011, respectively. She joined The University of Hong Kong, in 2010, as a Postdoctoral Fellow in computational electromagnetics (EM). She joined the Massachusetts Institute of Technology, in 2012, as a Postdoctoral Fellow in magnetic resonance imaging (MRI) related EM problems. She has been with the Pillar of Engineering Product Development, Singapore University of Technology and Design (SUTD), as an Assistant Professor, since 2014. She is currently an Adjunct Assistant Professor with the Department of Surgery, National University of Singapore, Singapore. Her research interests include radiofrequency (RF)/microwave noninvasive/contactless sensing, low-field MRI, non-linear MRI image reconstructions, RF aspects of MRI, wireless power transfer, and wideband RF/microwave components.